



저작자표시-비영리-변경금지 2.0 대한민국

이용자는 아래의 조건을 따르는 경우에 한하여 자유롭게

- 이 저작물을 복제, 배포, 전송, 전시, 공연 및 방송할 수 있습니다.

다음과 같은 조건을 따라야 합니다:



저작자표시. 귀하는 원저작자를 표시하여야 합니다.



비영리. 귀하는 이 저작물을 영리 목적으로 이용할 수 없습니다.



변경금지. 귀하는 이 저작물을 개작, 변형 또는 가공할 수 없습니다.

- 귀하는, 이 저작물의 재이용이나 배포의 경우, 이 저작물에 적용된 이용허락조건을 명확하게 나타내어야 합니다.
- 저작권자로부터 별도의 허가를 받으면 이러한 조건들은 적용되지 않습니다.

저작권법에 따른 이용자의 권리는 위의 내용에 의하여 영향을 받지 않습니다.

이것은 [이용허락규약\(Legal Code\)](#)을 이해하기 쉽게 요약한 것입니다.

[Disclaimer](#)

Impact of Arctic greening on the seasonality of local and remote climate

Yoojeong Chae

Department of Urban and Environmental Engineering
(Environmental Science and Engineering)

Graduate school of UNIST

2015

Impact of Arctic greening on the seasonality of local and remote climate

Yoojeong Chae

Department of Urban and Environmental Engineering
(Environmental Science and Engineering)

Graduate school of UNIST


Impact of Arctic greening on the seasonality of local and remote climate

A thesis
submitted to the Graduate School of UNIST
in partial fulfillment of the
requirements for the degree of
Master of Science

Yoojeong Chae

December 12, 2014

Approved by

A handwritten signature in black ink, appearing to read 'Sarah Kang', is written over a horizontal line.

Major Advisor
Sarah Kang

Impact of Arctic greening on the seasonality of local and remote climate

Yoojeong Chae

This certifies that the thesis by Yoojeong Chae is approved.

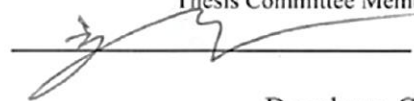
December 12, 2014



Sarah Kang
Assistant Professor of Urban and Environmental Engineering
Ulsan National Institute of Science and Technology
Thesis Committee Chairman



Myoung-in Lee
Associate Professor of Urban and Environmental Engineering
Ulsan National Institute of Science and Technology
Thesis Committee Member



Donghyun Cha
Assistant Professor of Urban and Environmental Engineering
Ulsan National Institute of Science and Technology
Thesis Committee Member

Abstract

With global warming, it is expected that vegetation type may also change, particularly in the northern high latitudes over the tundra region. Under a global warming scenario, grass and shrub type of vegetation are expected to shift to boreal forests over the Arctic. This study examines the impact of potential Arctic vegetation change with global warming on the seasonality of local Arctic and remote tropical climates, and compares its impact with the response to CO₂ doubling. Three experiments are performed with the NCAR Community Atmosphere Model 3 (CAM3) coupled to a slab ocean, which are perturbed by 1) Arctic vegetation change from grass and shrub to boreal forest with present day CO₂ concentrations (335ppmv), 2) present day vegetation type with doubling of CO₂, and 3) Arctic vegetation change to darker species with doubling of CO₂.

With darker vegetation over the Arctic, the Arctic region becomes warmer throughout the year due to the surface albedo reduction. However, because little insolation reaches the Arctic in boreal winter, the Arctic warming in boreal summer is four times greater than in boreal winter. Evapotranspiration changes also act to maximize the warming in boreal summer. In contrast, the Arctic warming peaks in November in response to a doubling of CO₂. As a result, as Arctic vegetation change is taken into consideration in addition to the doubling of CO₂, the peak of Arctic warming shifts to August, resulting in a weaker seasonality in the Arctic amplification.

Arctic warming driven by vegetation change results in imbalance of atmospheric energy budget between the hemispheres. Larger incoming insolation in the northern extra-tropics is balanced by increased outgoing longwave radiation (OLR) via warming the atmosphere, and some fraction reaches the subtropics by quasi-diffusive atmospheric eddy energy fluxes. As the northern subtropics become warmer relative to the southern subtropics, the Hadley circulation responds to transport energy southward across the equator because large horizontal temperature gradients cannot be sustained within the tropics due to the smallness of Coriolis parameter. Since the Hadley circulation transports energy in the direction of its upper branch, and moisture is transported northward across the equator, the time-mean inter-tropical convergence zone (ITCZ) is shifted northward. However, atmosphere cooling from June to September in local area can shift ITCZ to the south when Arctic incoming solar radiation is low.

Contents

ABSTRACT.....	V
CONTENTS.....	VI
LIST OF FIGURES	VII
CHAPTER 1.INTRODUCTION.....	1
CHAPTER 2. MODEL	3
CHAPTER 3. EXPERIMENTS.....	6
CHAPTER 4 RESULTS.....	8
4.1. Model and observation data	8
4.2. Local climate (Arctic amplification)	12
4.3. Remote climate (Tropical precipitation)	17
CHAPTER 5. CONCLUSIONS.....	28
REFERENCES.....	30

List of Figures

Figure 1 Model mixed layer depth.....	4
Figure 2 Map of annual mean (a) Control run Q-flux in slab ocean model which is the same as (b) model control. Positive (negative) indicates downward (upward).....	5
Figure 3 Plant Functional Types (PFTs) in (a) CNT and (b) VEG, with green and yellow corresponding to boreal forest and shrub/grasslands, respectively. (c) Monthly Leaf Area Index (LAI) averaged poleward of 60°N in CNT (blue) and in VEG (red).....	7
Figure 4 Annual mean precipitation (mm/day) (a) control run (CNT), (b) GPCP observation (OBS), and the difference between (c) CNT and OBS.....	9
Figure 5 Annual mean Top of atmosphere (TOA) SW and LW (W/m^2) (a) control run (CNT), (b) GPCP observation(OBS), and the difference between (c) CNT and OBS. Positive indicates downward fluxes.....	9
Figure 6 Annual mean Surface (SFC) SW and LW (W/m^2) (a) control run (CNT), (b) GPCP observation(OBS), and the difference between (c) CNT and OBS. Positive indicates upward fluxes.....	10
Figure 7 Annual mean High and Low cloud fraction (a) control run (CNT), (b) GPCP observation(OBS), and the difference between (c) CNT and OBS.....	11
Figure 8 (a) The response of annual-mean zonal-mean 950hPa temperature to vegetation change (blue), CO ₂ doubling (red), and both vegetation and CO ₂ doubling (black). The sum of blue and red is shown with the black dashed line. The shading indicates plus/minus one standard deviation. The map of annual-mean 950hPa temperature change to (b) vegetation, (c) CO ₂ doubling, and (d) both vegetation and CO ₂ doubling.....	13
Figure 9 Monthly response averaged poleward of 60°N of (a) 950hPa temperature, (b) surface albedo, and (c) sea ice fraction, to vegetation change (blue), doubling of CO ₂ (red), and both vegetation and CO ₂ doubling (black). The sum of blue and red is shown with the black dashed line. The shading indicates plus/minus one standard deviation.	14
Figure 10 Monthly response averaged poleward of 60°N in VEG of net shortwave radiation (SW, red), net longwave radiation (LW, blue), sensible heat fluxes (SH, cyan), latent heat fluxes (LH, pink), and evapotranspiration (ET, dashed pink). Positive indicates downward fluxes.	16
Figure 11 The annual-mean response of (a) 2m temperature (K) and (c) precipitation (mm/day). (b, d) The zonal-mean of (a, c) in MAM, JJA, SON, and DJF in pink, red, cyan, and blue, respectively.	18
Figure 12 Annual mean Hadley cell of CNT (black line) and VEG (shading). Black dashed and blue shading corresponds to count clockwise, and black solid indicates clockwise circulation.....	19
Figure 13 Annual mean atmospheric energy transports in CNT (black) and its change in VEG (red) in W. Positive (negative) indicates northward (southward) energy transport.	20
Figure 14 Annual mean moisture transports in CNT (black) and its change in VEG (red) in W. Positive (negative) indicates northward (southward) moisture transport.....	21
Figure 15 The change in atmospheric energy transport between 15S and 15N (F_0 in PW, blue), the change in precipitation asymmetry index (δPAI , green), and the energy flux equator (θ_e , red) in VEG.	22

Figure 16 The column atmospheric energy budget for each season (in 1013 PW). Blue (red) corresponds to cooling (warming) the atmospheric column, and black denotes the direction of atmospheric energy transport.....	24
Figure 17 Seasonal map of total atmospheric energy budget (TOT NET in W/m^2), which is the sum of net downward TOA radiative fluxes (R_{TOA}) and net upward surface energy fluxes (R_{SFC}). Red and blue corresponds to warming and cooling the atmosphere.	25
Figure 18 Seasonal map of top-of- atmospheric energy budget (TOT NET in W/m^2). Red and blue corresponds to warming and cooling the atmosphere.	25
Figure 19 Seasonal maps of short wave cloud forcing (SWCF in W/m^2). Red and blue corresponds to warming and cooling the atmosphere.	26
Figure 20 Seasonal map of surface energy budget (SFC NET in W/m^2). Red and blue corresponds to warming and cooling the atmosphere.	26
Figure 21 Seasonal map of TOA SW in clear sky (W/m^2). Red and blue corresponds to warming and cooling the atmosphere	27

Chapter 1.Introduction

Since the beginning of the twentieth century, Arctic surface temperature has increased at twice the rate of global mean temperature (IPCC AR4, 2007). This feature, referred to as Arctic amplification, is ubiquitous in climate models and observations (e.g. Manabe and Stouffer 1980, Serreze and Barry 2011). Based on CMIP 3 models, Winton (2006) find a mean annual Arctic warming that is 1.9 times greater than the global mean warming at the time of CO₂ doubling. One of the key features of amplified Arctic warming is a pronounced seasonality as winter warming exceeds summer warming by at least a factor of 4 (Bintanja and van der Linden 2013).

There have been numerous studies on the Arctic amplification. The importance of Arctic amplification is that arctic climate change can affect not only high latitude but also mid latitude. Francis et al., (2012) suggest that Arctic warming is linked to extreme weather in mid latitudes. Polar warming is related with poleward thickness gradient, and it contributes to weak zonal wind and increase Rossby wave amplitude. In high latitude, polar warming related to earlier snow and ice melting.

In response to Arctic warming, high latitude biome apparently changed with habitat migration (Sturm et al., 2001), longer growing season (Jeong et al., 2011), and enhanced photosynthetic activity (Xu et al., 2013). These are generally considered as an evidence of the Arctic “greening”. Specifically, over the past century, ground observation data show that fraction of vegetation has been increasing, especially in the Arctic tundra where extension of shrub area is prominent (Tape et al., 2006; Bunn et al., 2006; Sturm et al., 2001; Potter et al., 2013). Especially, Pearson et al (2013) reported Arctic area have experienced significant changes in vegetation composition including a northward migration of the Arctic tree-line during the last several decades. In line with observed relationships between warming and biome changes, future model projection also predicts circumpolar greening with a northward expansion of boreal forest and enhanced greenness of tundra regions in the future climate with increasing CO₂ (Notaro et al., 2007; Jeong et al. 2011, hereafter JSJ11).

The vegetation greening in the high-latitudes in a warmer climate can amplify Arctic warming by two to seven times due to decreased surface albedo (Chapin et al., 2005). Transpiration of water vapor and feedbacks from the ocean and sea-ice also contributes to amplifying high-latitude warming (Swann et al., 2010; hereafter ALS10, Lorant et al., 2011). These studies confined the analysis to the annual-mean. Although vegetation may change throughout the year, its effect on the Arctic climate may exhibit large seasonality as there is no sunlight to reflect during polar night. Therefore, we study how Arctic vegetation change affects the seasonality of Arctic amplification.

The Arctic vegetation changes resulting from global warming makes energy imbalance between hemispheres, so it can affect not only local but also remote climate such as ITCZ. ITCZ is zonal rainfall maximum area in tropics and located the north or south of the equator. Although annual mean

solar radiation is symmetric to the equator but atmospheric conditions are asymmetric between hemispheres, therefore, the location of ITCZ is changed. Previous studies show that ITCZ is controlled by tropical mechanisms such as cold waters at the tropics (Pike et al., 1971), the flow of thermocline water from the subtropical (Lu and McCreary, 1995). However, recently numerous studies also have investigated that any climate forcing agents that cause hemispheric asymmetry in atmospheric energy budget regardless of its latitudinal position can shift the latitude of the ITCZ meridionally (Kang et al., 2008, 2009, Seo et al., 2014). ITCZ shift due to energy imbalance between hemispheres also has been shown in coupled model by the case of northern hemisphere cooling (Broccoli et al., 2006). Consistent with this, several studies have investigated that local vegetation change could affect the shift of mean tropical precipitation. For example, afforestation in the Northern Hemisphere (NH) middle latitude is shown to induce a northward shift of the annual-mean ITCZ (Swann et al., 2012), and expanded forest cover in the mid-Holocene relative to today is shown to shift the ITCZ northward resulting in an increased precipitation over Northern Africa with the most pronounced response in boreal summer (Swann et al., 2014). However, since the thermal forcing caused by Arctic vegetation change has a clear seasonal trend because no sunlight reaches the Arctic region in boreal winter, it is expected that the impact of Arctic vegetation change on the ITCZ location to vary with season as global warming.

Therefore, in this study, we investigate the impact of Arctic greening on the seasonality of Arctic amplification and the ITCZ location. JSJ11 shows that the land surface temperature response to vegetation change is sensitive to its latitudinal position. In the middle latitudes, increasing vegetation limits the warming trend due to increased evapotranspiration, whereas that in the high latitudes reinforces the warming trend due to the reduced surface albedo. To avoid complications from these contrasting effects, we only consider vegetation type changes poleward of 60°N.

Chapter 2. Model

The global climate model (GCM) used in this study is the National Center for Atmospheric Research (NCAR) Community Atmospheric Model version 3 (CAM3; Collins et al., 2004). It includes options for Eulerian spectral, semi-Lagrangian, and finite-volume formulations of the dynamical equations. It supports coupled simulations using either finite-volume or Eulerian dynamics via an explicit set of adjustable parameters governing the model time step, cloud parameterizations, or condensation processes (Collins et al., 2006). Hurrell et al. (2006) was examined dynamical simulation of CAM3 including the seasonal variation.

The model is configured with spectral T42 ($2.875^\circ \times 2.875^\circ$) horizontally and 26 hybrid-sigma levels in the vertical. This model is coupled to a slab ocean, with spatially varying mixed layer depth where the sea surface temperatures (SSTs) freely evolve to ensure that the surface energy budget is closed.

CAM3 model was used in various simulations such as the role of the interaction between deep and shallow convection in MJO simulation (Zhang and Song, 2009) and indirect effect of aerosols on cold clouds (Liu et al., 2007). CAM3 has been evaluated based on surface, satellite, and reanalysis data by Collier and Zhang (2007). Updated convective scheme version of CAM 3 is CAM 3.5 (Chen et al., 2010) was evaluated by Gent et al. (2010) as well.

Land-surface processes in CAM3 are calculated with the Community Land Model version 3 (CLM3; Oleson et al., 2004) that calculates the heat, moisture, and momentum fluxes between land surfaces and atmosphere as well as the thermal and hydrologic processes at the surface and the interior of near-surface soil layer.

Coupled with CAM3 at a T42 horizontal resolution, CLM3 is comprised of 3,799 grid points. Four primary land cover types which are glacier, lake, wetland, and. The vegetated portion of the grid cell is represented by the fractional coverage of plant functional types (PFTs). The model uses seven PFTs: namely, needle-leaf evergreen or deciduous trees, broadleaf evergreen or deciduous trees, deciduous shrubs, grass, and crops. In each PFT, leaf phenology in the CLM3 is prescribed, and the seasonal course of leaf area index (LAI) for each PFT is derived through interpolating the monthly PFT-specific LAI from National Oceanic and Atmospheric Administration (NOAA) Advanced Very High Resolution Radiometer (AVHRR) data. We prescribed annual mixed layer depth as Figure 1, and it has no seasonality. To make energy balance, we used slab ocean model which contains Qflux which also can indicated in minus surface net fluxes represents seasonal deep water exchange and horizontal heat transport (Figure 2). The model is integrated for 100 years, and we use the mean of last 80 years as an equilibrium state.

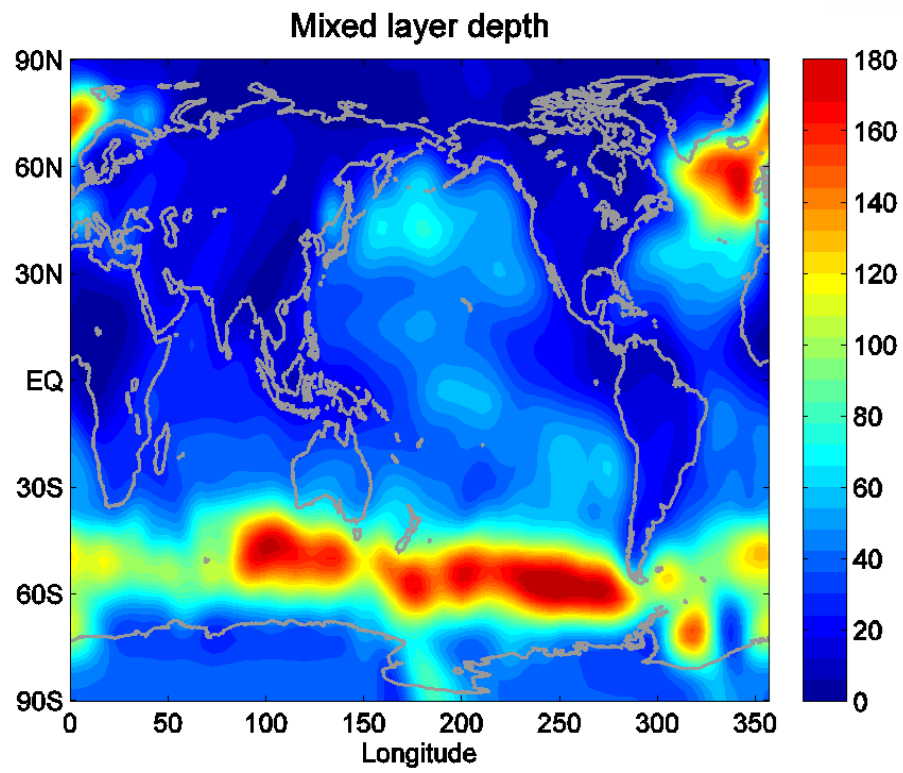


Figure 1 Model mixed layer depth

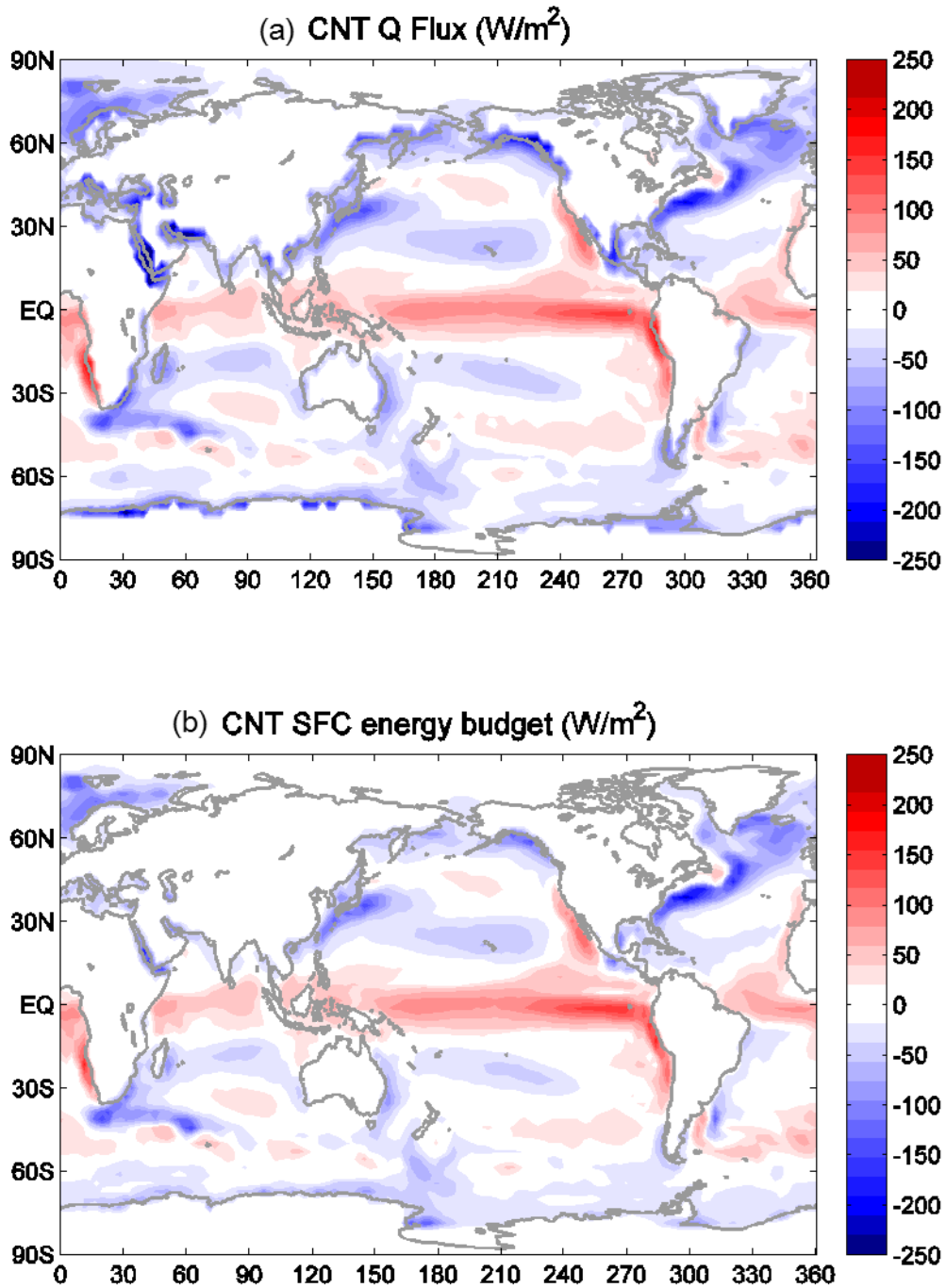


Figure 2 Map of annual mean (a) Control run Q-flux in slab ocean model which is the same as (b) model control. Positive (negative) indicates downward (upward).

Chapter 3. Experiments

The control integration, denoted as CNT, is with the present-day CO₂ concentration (335ppmv) and the vegetation type fixed to the current climate distribution. It is the hypothetical vegetation state that would occur in the absence of human influences (e.g., urbanization, deforestation, and change to cultivated area), which is obtained by running CAM3 with the dynamic global vegetation model (DGVM) (Levis et al., 2004) where the SSTs and sea ice distributions (SICs) are fixed to the climatological mean over the period 1950-2000 from the Hadley Center data. The PFT in CNT shown in Figure 3a indicates that shrub and grass are dominant vegetation types poleward of 60°N. In response to doubled CO₂ concentration, most northern high latitude regions with grass and shrub are suggested to be replaced with boreal forest (JSJ11). Hence, the effect of poleward expansion of forest with global warming is studied by replacing grass/shrub poleward of 60°N in CNT with boreal forest, as shown in Figure 3b. In the study by JSJ11, the model is run with fixed SST and SICs (to that derived from the ocean-atmosphere coupled model, CCSM3, under either present-day or doubled CO₂ condition), whereas in our study the SST and SICs are allowed to adjust. Monthly LAI in Figure 3c indicates that there is distinct growing season of shrub and grass type from May to September in CNT (blue), but under double CO₂ (red), vegetation exists all year long, especially increasing from June to November.

In order to differentiate the response to direct CO₂ radiative forcing and that to Arctic vegetation change, three perturbed experiments have been performed: (1) with the present-day CO₂ concentration and altered vegetation type only poleward of 60°N (denoted as VEG), (2) with CO₂ doubled, but vegetation fixed to present-day condition (denoted as 2CO₂), and (3) with CO₂ doubled and altered vegetation type poleward of 60°N (VEG+2CO₂). We analyze the difference between the perturbed and the control integrations.

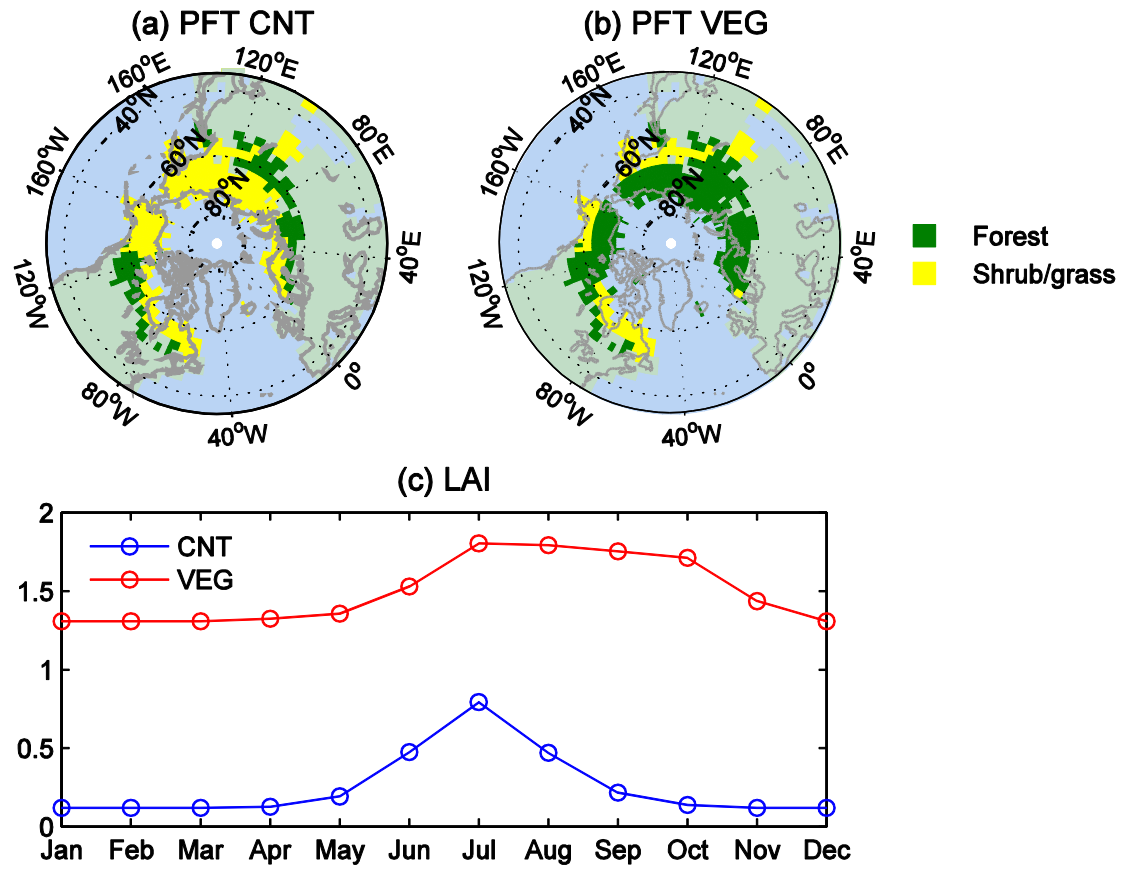


Figure 3 Plant Functional Types (PFTs) in (a) CNT and (b) VEG, with green and yellow corresponding to boreal forest and shrub/grasslands, respectively. (c) Monthly Leaf Area Index (LAI) averaged poleward of 60°N in CNT (blue) and in VEG (red).

Chapter 4 Results

4.1. Model and observation data

Chapter 4.1 describes model validation as comparing model control run with observation data. Model validation is important because it is related with reliability of model results. Each Figure 4-7 show model control run (CNT, left) and GPCP observation (OBS, middle) and the difference between CNT and OBS (right) of each variable. Our model underestimated where precipitation high region (Figure 4), however, the differences of SW between model and observation are balanced in TOA and SFC (Figure 5, 6). This model generally overestimated LW and cloud fraction than observation data (Figure 5, 6, 7).

Precipitation

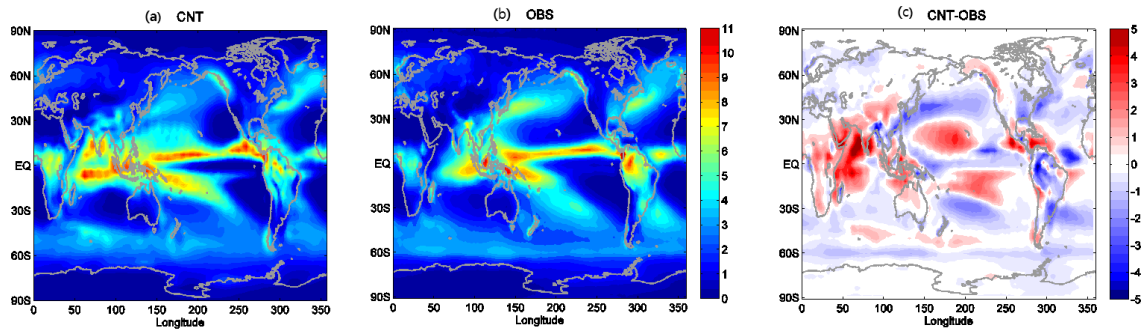
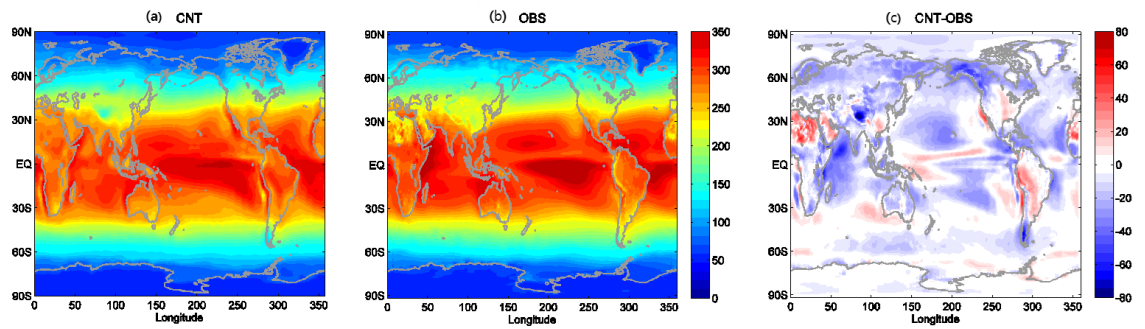


Figure 4 Annual mean precipitation (mm/day) (a) control run (CNT), (b) GPCP observation (OBS), and the difference between (c) CNT and OBS.

TOA SW



TOA LW

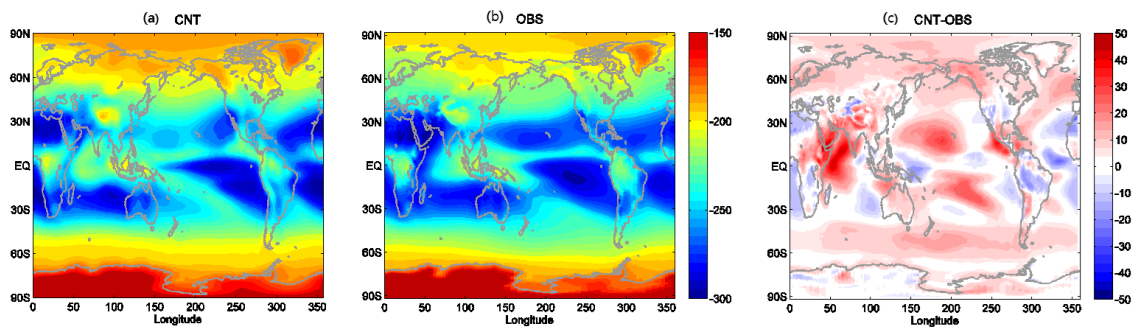
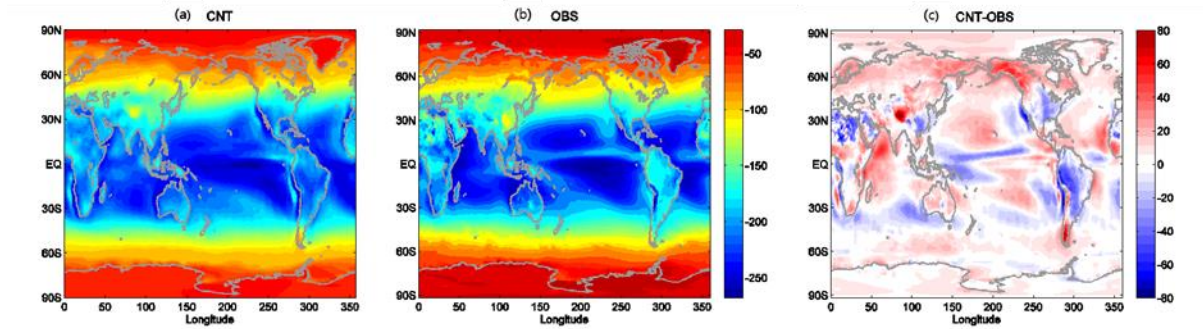


Figure 5 Annual mean Top of atmosphere (TOA) SW and LW (W/m^2) (a) control run (CNT), (b) GPCP observation (OBS), and the difference between (c) CNT and OBS. Positive indicates downward fluxes.

SFC SW



SFC LW

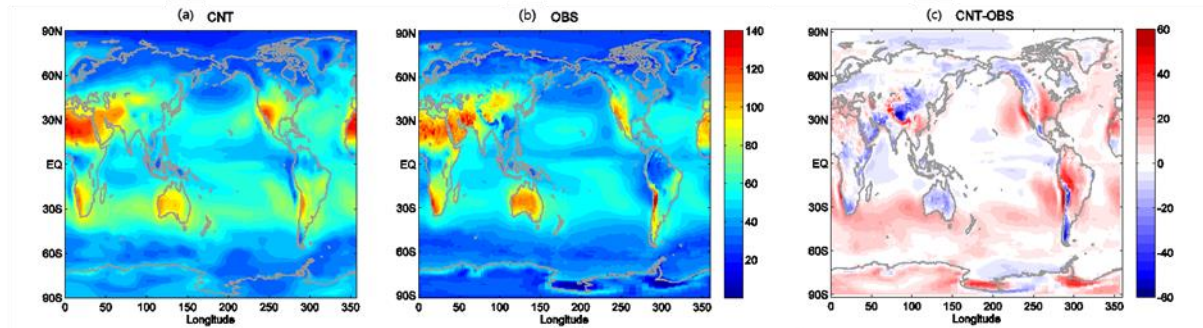
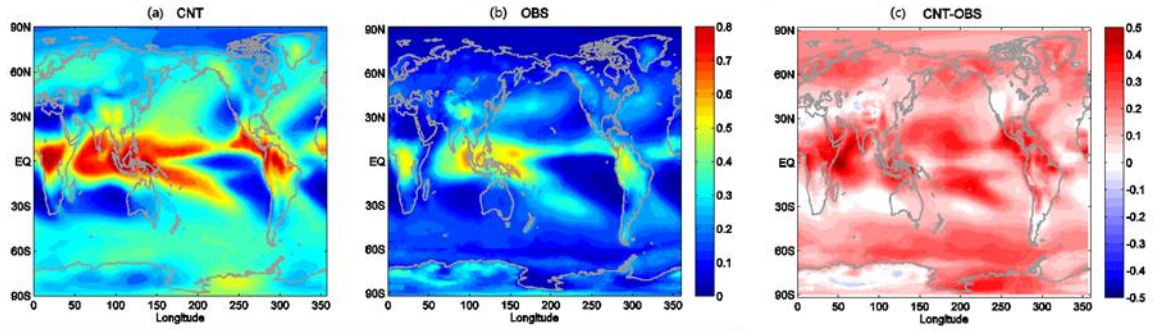


Figure 6 Annual mean Surface (SFC) SW and LW (W/m²) (a) control run (CNT), (b) GPCP observation(OBS), and the difference between (c) CNT and OBS. Positive indicates upward fluxes.

High cloud fraction



Low cloud fraction

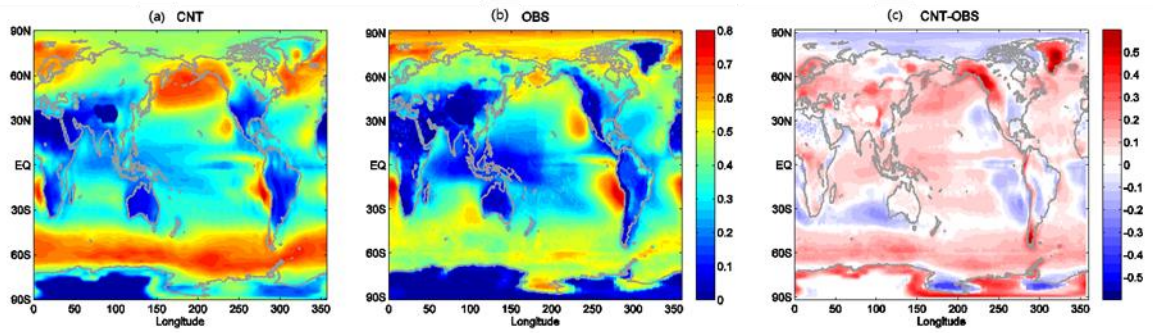


Figure 7 Annual mean High and Low cloud fraction (a) control run (CNT), (b) GPCP observation(OBS), and the difference between (c) CNT and OBS.

4.2. Local climate (Arctic amplification)

Figure 8 shows the simulated annual-mean change in temperature at 950hPa (T950). We note that the following discussion qualitatively holds for all vertical levels below 800hPa. In response to CO₂ doubling (red) the polar regions warm twice as much as the tropics, with the similar magnitude of warming at both poles. In response to Arctic vegetation change (blue), the annual-mean temperature increases by 2.3 K poleward of 60°N, with a peak at 65°N where land albedo is changed most. The spatial pattern of warming is shown in Figures 8(b)-8(d). In a study by ALS10 where the effect of Arctic vegetation changes is investigated by adding deciduous forest on bare ground at high northern latitudes, the near surface Arctic warms by only 1 K in the annual-mean. The contrast stems from the difference in experiment setup: in our study compared to ALS10, larger reduction in surface albedo is induced by 2 and 5 times and larger increase in transpiration (that induces larger water vapor feedback) is induced by 1.5 and 20 times in April and July, respectively. The sum of the responses in VEG and 2CO₂ (black dashed) almost coincides with the response in VEG+2CO₂ (black). This linearity holds at every month with high accuracy (Figure 9a), allowing a decomposition of the response in VEG+2CO₂ into the responses to CO₂ doubling and Arctic vegetation change. One third of the annual-mean T950 increase poleward of 60°N in VEG+2CO₂ results from VEG, but its relative contribution varies with month. The contribution from VEG reaches 55% during the growing season and falls to 11% in boreal winter.

Figure 9a shows the monthly changes in T950 averaged poleward of 60°N in all experiments. In 2CO₂ (red), the warming response over the northern high latitudes is largest in November, and smallest in June, consistent with the CMIP5 simulated response to increased CO₂ (Pithan and Mauritsen et al., 2014). The maximized warming occurs in fall and early winter because most incoming solar radiation in summer is taken up to melt the ice and warm areas of open ocean whereas during late fall and winter ocean transfers heat to the atmosphere (Screen and Simmonds 2010). In VEG (blue), during the growing season, Arctic warming is intensified by 3.5 K, 20% larger than the response in 2CO₂. The predominant temperature increase during the growing season is due to reduced surface albedo from vegetation type change (Figure 9b). In fact, there are two peaks in the surface albedo reduction, one in May associated with land greening and the other in October associated with sea ice melt (Figures 9b and 9c).

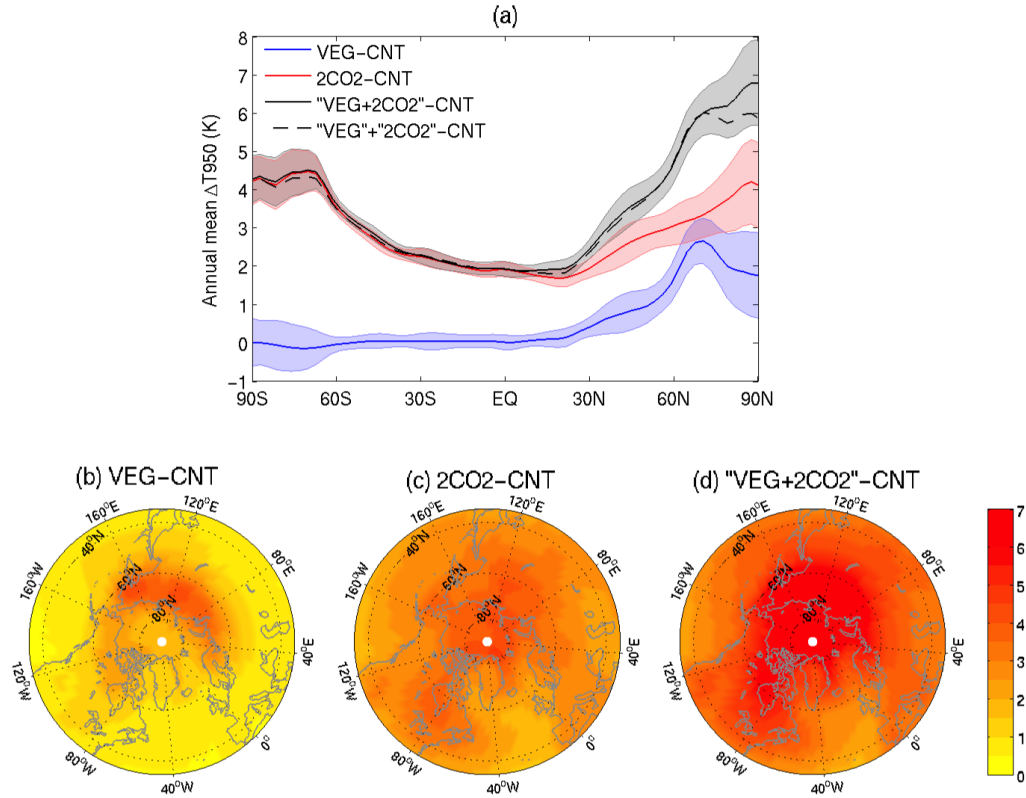


Figure 8 (a) The response of annual-mean zonal-mean 950hPa temperature to vegetation change (blue), CO2 doubling (red), and both vegetation and CO2 doubling (black). The sum of blue and red is shown with the black dashed line. The shading indicates plus/minus one standard deviation. The map of annual-mean 950hPa temperature change to (b) vegetation, (c) CO2 doubling, and (d) both vegetation and CO2 doubling.

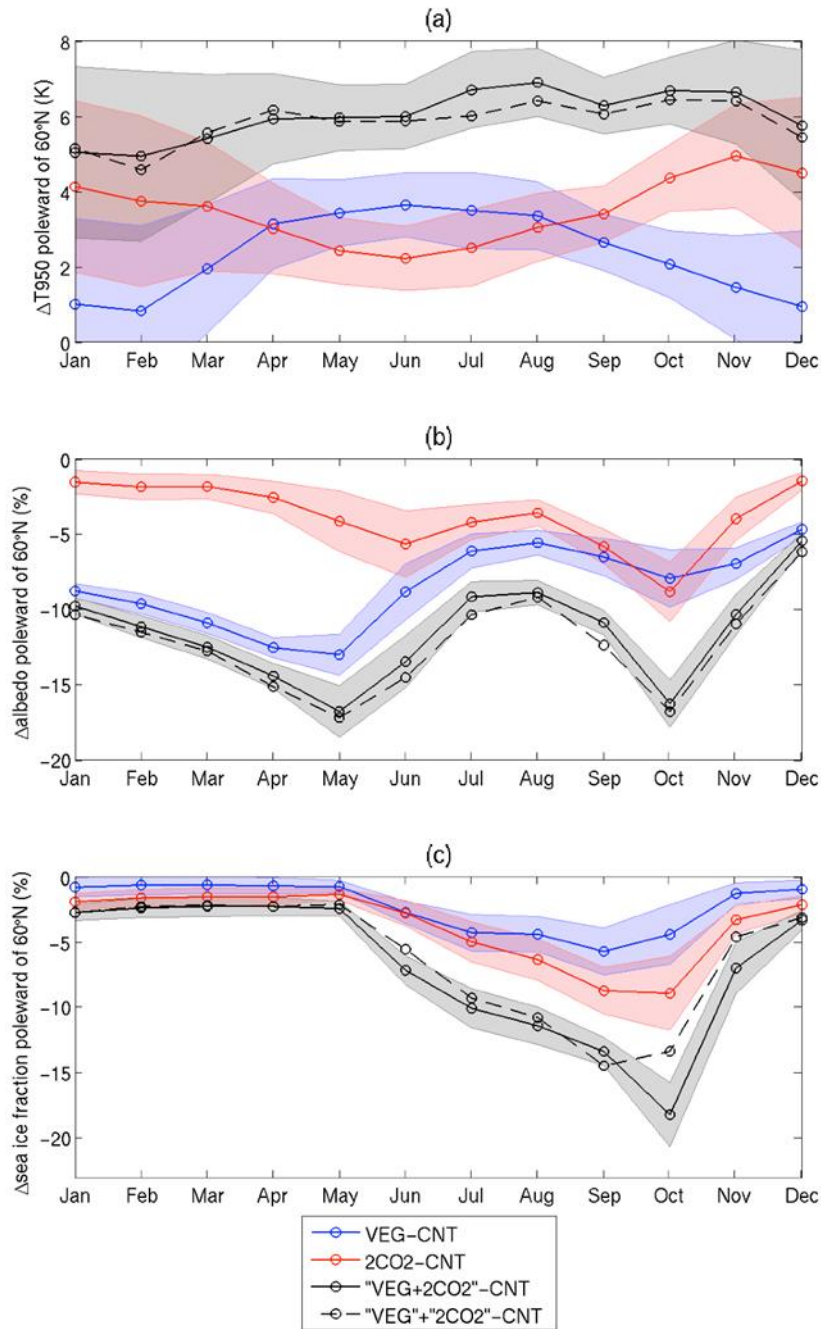


Figure 9 Monthly response averaged poleward of 60°N of (a) 950hPa temperature, (b) surface albedo, and (c) sea ice fraction, to vegetation change (blue), doubling of CO₂ (red), and both vegetation and CO₂ doubling (black). The sum of blue and red is shown with the black dashed line. The shading indicates plus/minus one standard deviation.

However, since little sunlight reaches the high latitudes in late fall and winter, the reduced albedo in late fall does not yield more incoming solar radiation (Figure 10). Hence, although vegetation is changed throughout the year, the amount of insolation reaching the Arctic surface is most enhanced in June. Moreover, as ALS10 suggested, the greenhouse warming by additional atmospheric water vapor content resulting from enhanced evapotranspiration in the summer (dashed pink) can contribute to a maximized warming during the growing season. In ALS10, the radiative forcing of enhanced water vapor from evaporation is shown to be of the same order of magnitude as shortwave forcing from albedo reduction. However, in our experiment setup with larger changes in albedo, we expect the effect of a decrease in albedo to overwhelm the effect of an increase in water flux from transpiration, as implied in Figure 10.

It is large seasonality in the incoming solar radiation over the Arctic that causes large seasonal variation in the net shortwave flux at the surface and evapotranspiration. As a result, when vegetation change is considered in addition to doubling of CO₂ (black in Figure 9a), the Arctic amplification is maximized earlier than when only CO₂ doubling is accounted for, leading to a weaker seasonality.

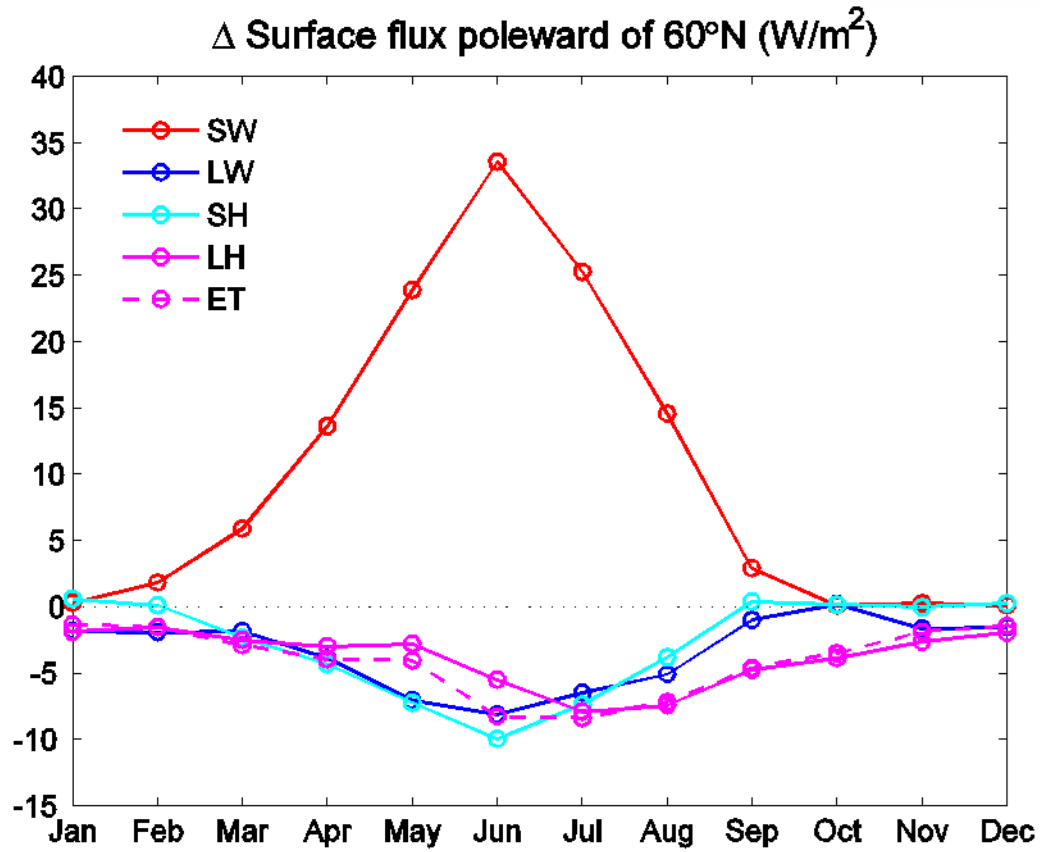


Figure 10 Monthly response averaged poleward of 60°N in VEG of net shortwave radiation (SW, red), net longwave radiation (LW, blue), sensible heat fluxes (SH, cyan), latent heat fluxes (LH, pink), and evapotranspiration (ET, dashed pink). Positive indicates downward fluxes.

4.3. Remote climate (Tropical precipitation)

Figure 11a shows the annual-mean response of 2m temperature in VEG. As vegetation is changed poleward of 60°N, the Arctic region becomes warmer by 4 K in the annual-mean (Figure 11a). Heating over the Arctic is fluxed into the lower latitudes by the quasi-diffusive eddies, and the northern mid-latitudes become warmer by 1 K. As the northern subtropics become warmer than the southern subtropics, the anomalous Hadley circulation (HC) is induced that transports energy southward across the equator (Figure 12, Figure 13) in order to flatten the upper tropical tropospheric temperature (Kang et al. 2009). Following the direction of the lower branch of the HC, moisture is then transported northward across the equator, leading to a northward shift of the ITCZ (Figure 14). Figure 11c indeed shows that Arctic vegetation change moistens the northern tropics and dries the southern tropics, consistent with Swann et al. (2010).

As discussed in Section 4.1, since the magnitude of insolation reaching the Arctic is greatly season dependent, the Arctic temperature response is a strong function of season, and so is the magnitude of perturbation reaching the lower latitudes (Figure 11b). In particular, the northern mid-latitude warming response is maximized in June-July-August (JJA). However, Figure 11d shows that the tropical precipitation response is largest in March-April-May (MAM). Following Hwang and Frierson (2013), the seasonal contrast in the tropical precipitation response is quantified by a tropical precipitation asymmetry index (PAI) defined as:

$$PAI = \frac{P(Eq-15^{\circ}N) - P(15^{\circ}S-Eq)}{P(15^{\circ}S - 15^{\circ}N)}$$

Positive change in PAI corresponds to a northward shift of tropical precipitation, and vice versa. The PAI response with season is shown in Figure 15 in green. The largest northward shift occurs in MAM, and, interestingly, there is a slight southward shift in September-October-November (SON).

The tropical precipitation response mostly results from the response of moisture convergence by the anomalous Hadley mass transport. Hence, PAI is expected to be proportional to the magnitude of anomalous atmospheric energy transport in the deep tropics, denoted as δF_0 , calculated as the average of the response of atmospheric energy transport, F , over 15°S to 15°N (Kang et al. 2008). F is the vertical integral of meridional flux of moist static energy, which can be alternatively computed from the equation for the steady-state atmospheric energy budget, $R_{TOA} + R_{SFC} = \nabla \cdot F$ where R_{TOA} is downward top-of-atmosphere (TOA) net radiation and R_{SFC} is the upward net surface radiation. In turn, F_0 is proportional to the zero-crossing latitude of atmospheric transport F , referred to as the

energy flux equator θ_e in Kang et al. (2008). To quantify the seasonal dependence of tropical precipitation response, Figure 15 compares the PAI change (green), δF_0 (blue), and θ_e (red) with season. δF_0 and θ_e nicely predicts the seasonality of tropical precipitation response.

In order to understand the seasonal dependence of δF_0 , the response of column atmospheric energy budget is examined.

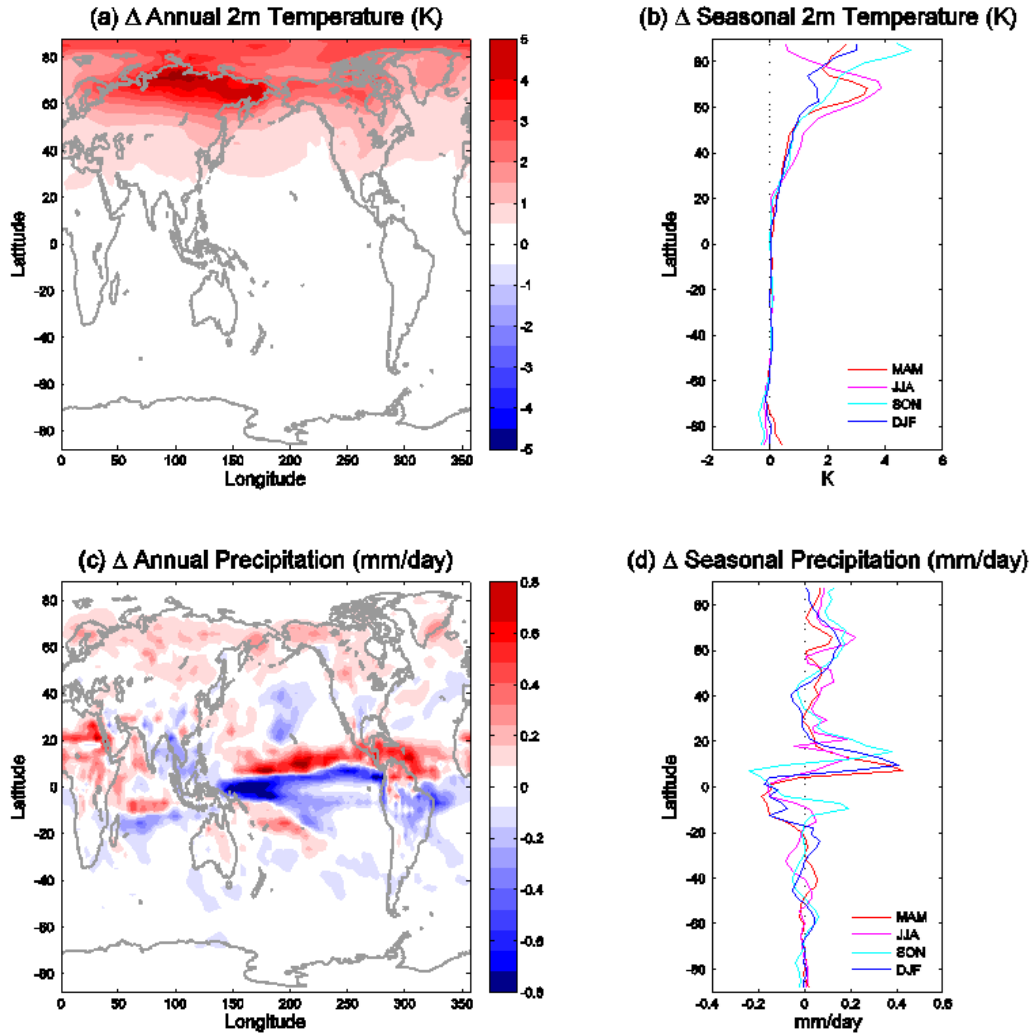


Figure 11 The annual-mean response of (a) 2m temperature (K) and (c) precipitation (mm/day). (b, d) The zonal-mean of (a, c) in MAM, JJA, SON, and DJF in pink, red, cyan, and blue, respectively.

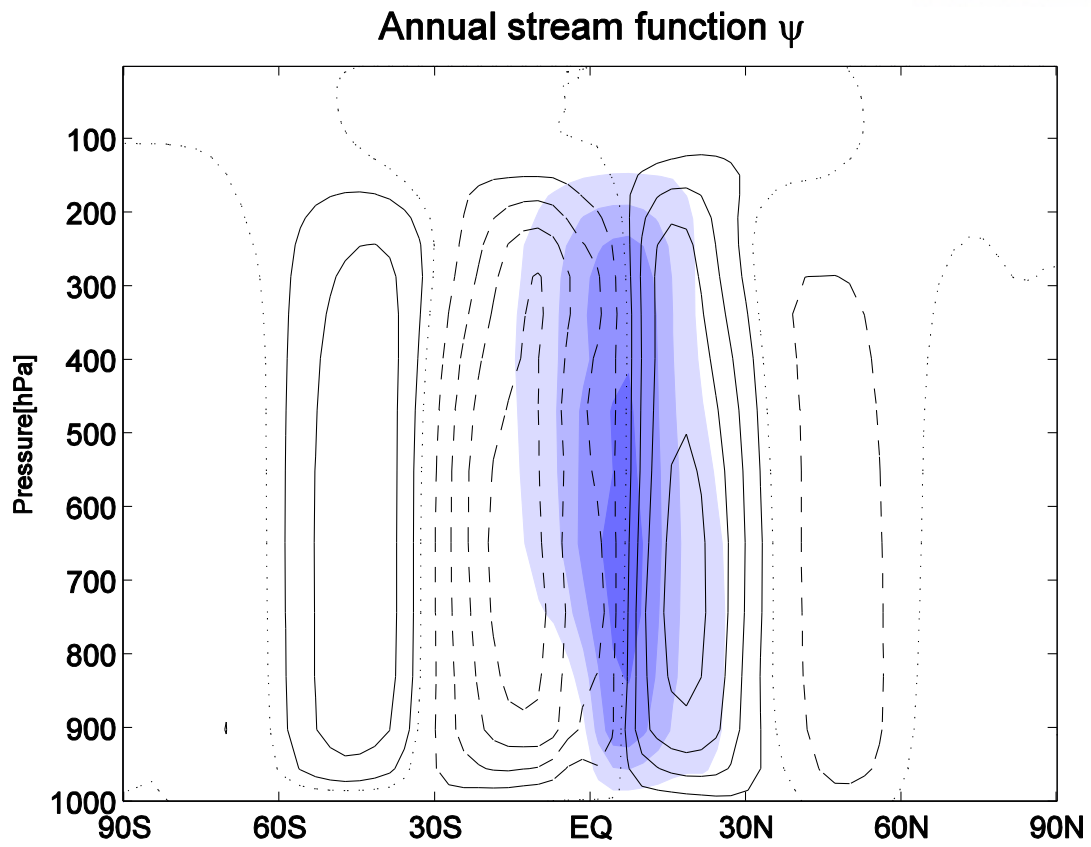


Figure 12 Annual mean Hadley cell of CNT (black line) and VEG (shading). Black dashed and blue shading corresponds to count clockwise, and black solid indicates clockwise circulation.

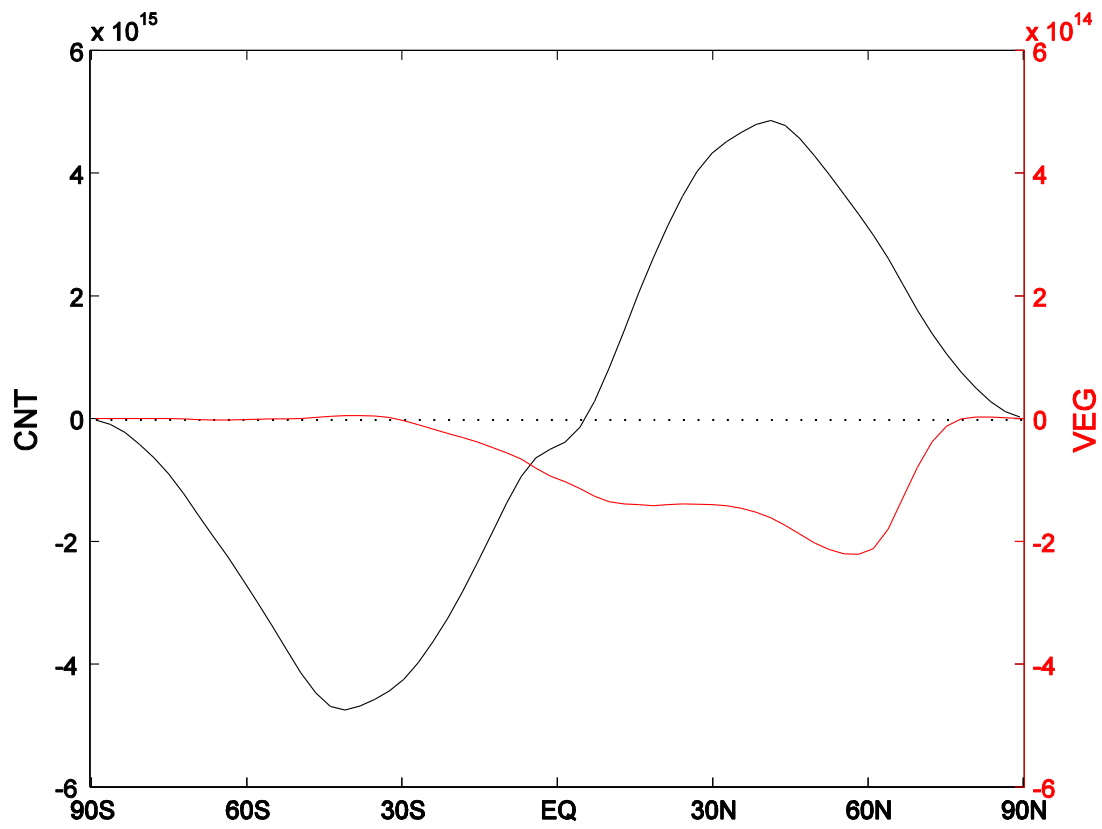


Figure 13 Annual mean atmospheric energy transports in CNT (black) and its change in VEG (red) in W. Positive (negative) indicates northward (southward) energy transport.

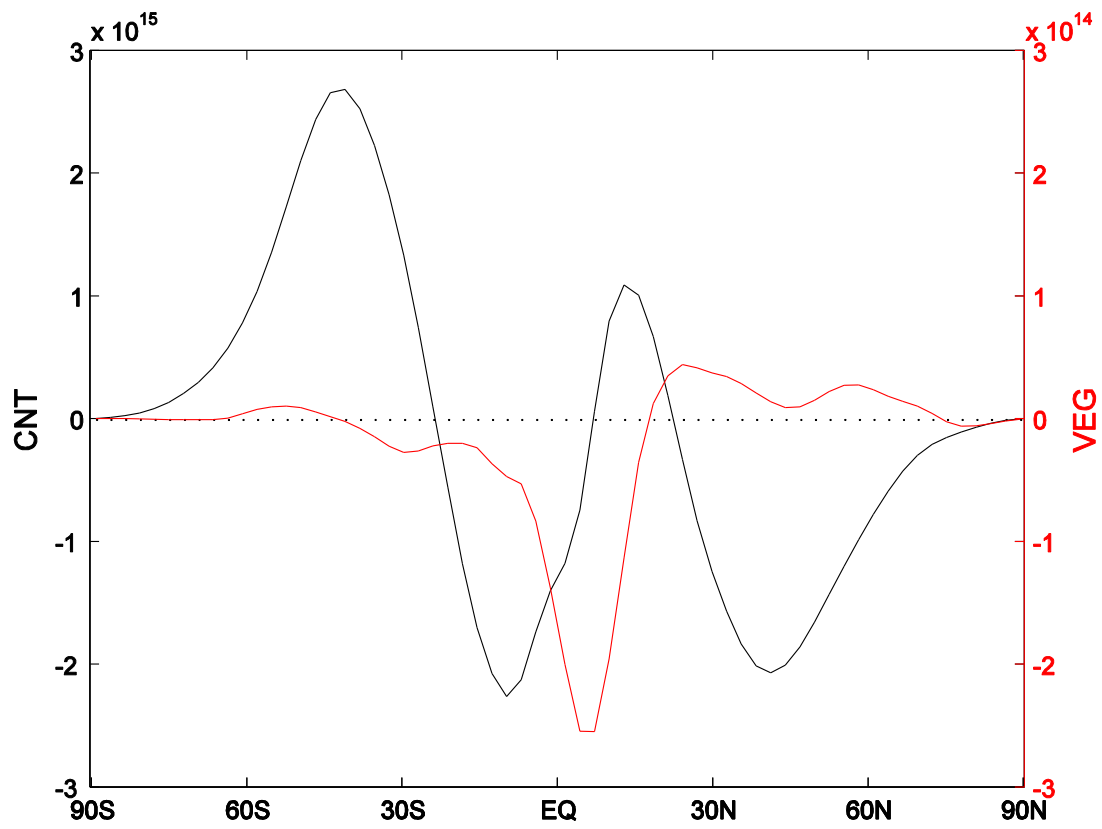


Figure 14 Annual mean moisture transports in CNT (black) and its change in VEG (red) in W. Positive (negative) indicates northward (southward) moisture transport.

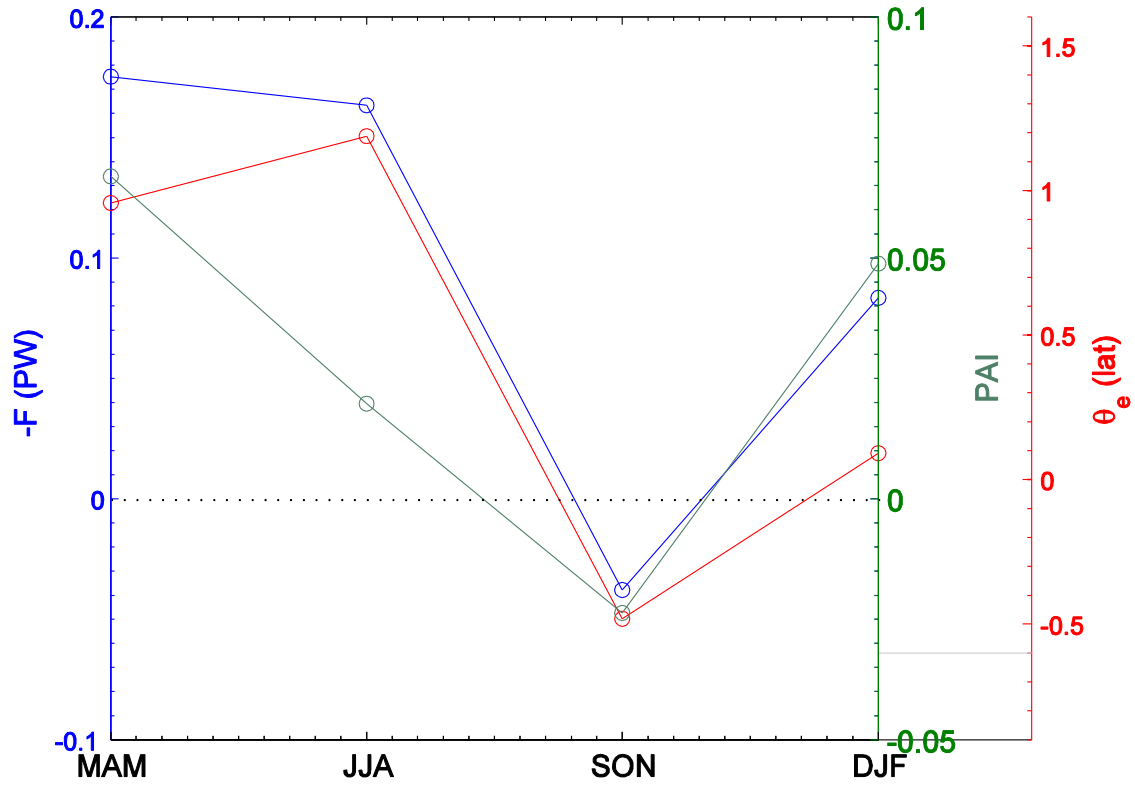


Figure 15 The change in atmospheric energy transport between 15S and 15N (F_0 in PW, blue), the change in precipitation asymmetry index (δ PAI, green), and the energy flux equator (θ_e , red) in VEG.

To understand which forcing can make the largest northward ITCZ shift in MAM (via F and PAI) and southward ITCZ shift in SON, we analysis the seasonality box plot of R_{TOA} , R_{SFC} , $\nabla \cdot F_A$ (Figure 16), and map (Figure 17).

In MAM and JJA, clear sky incoming SW is larger in TOA and smaller increasing surface downward SW in TOA due to albedo decreasing poleward of 60°N. The surplus of energy move to the south, and most of it is transported to the south across the equator. However, In JJA and SON, the cooling exists over the North Pacific located in middle latitude which reduces southward atmospheric energy transport. The cooling can make more energy transport to the south in equator in MAM than JJA. To understand the cooling, Figure 17 can be divided into R_{TOA} (TOA NET) (Figure 18) and R_{SFC} (SFC NET) (Figure 20).

Figure 12 and 14 show that cooling over the North Pacific is caused by TOA NET 8h Pacific is due to reduced SW cloud forcing (SWCF) (Figure19) by low and high cloud increasing in JJA. However, cooling over the North Pacific in SON and heating in DJF can be considered SFC NET. Since incoming isolation is very small in SON and DJF (Figure 16). Therefore, cooling in SON is can over-compensates Arctic heating. Therefore, in SON, ITCZ is shifted southward even heating exist in the high latitude. Our results show that the arctic greening can move ICTZ shift but it is from different energy sources between spring, summer and fall, winter.

Δ Atmospheric energy transport (10^{13}W)

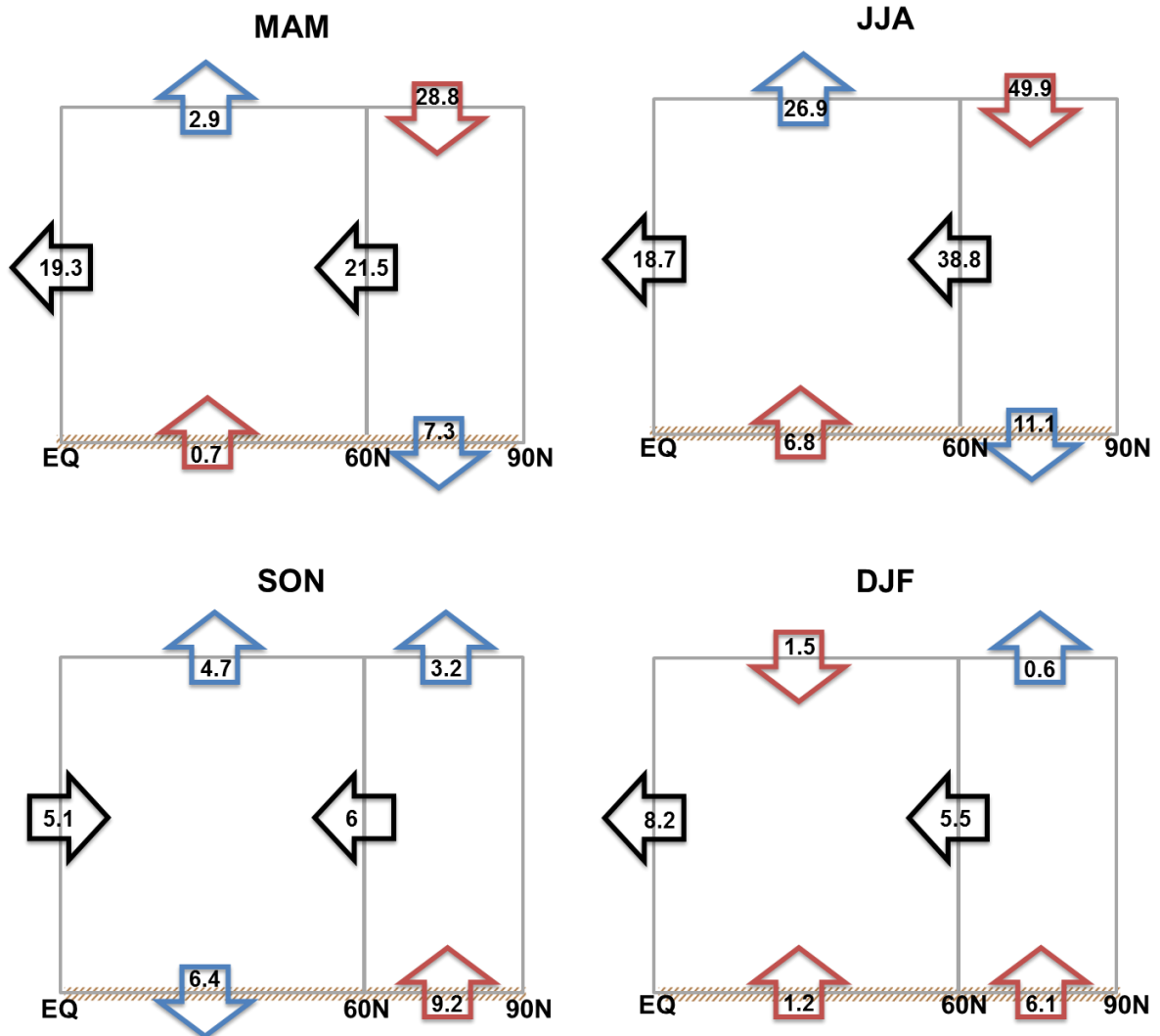


Figure 16 The column atmospheric energy budget for each season (in 10^{13}PW). Blue (red) corresponds to cooling (warming) the atmospheric column, and black denotes the direction of atmospheric energy transport

TOT NET

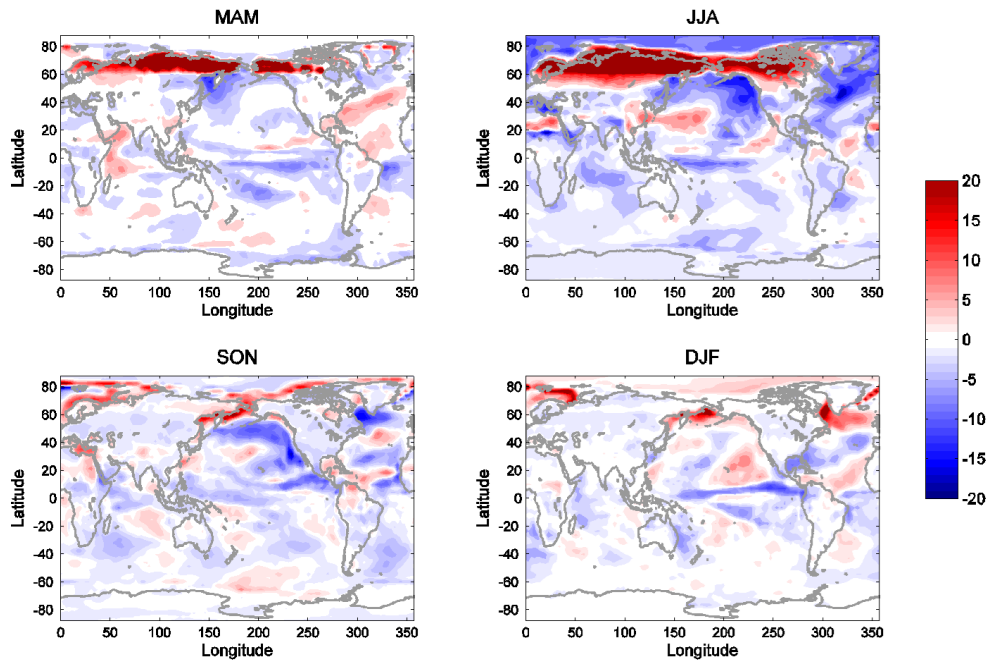


Figure 17 Seasonal map of total atmospheric energy budget (TOT NET in W/m^2), which is the sum of net downward TOA radiative fluxes (R_{TOA}) and net upward surface energy fluxes (R_{SFC}). Red and blue corresponds to warming and cooling the atmosphere.

TOA NET

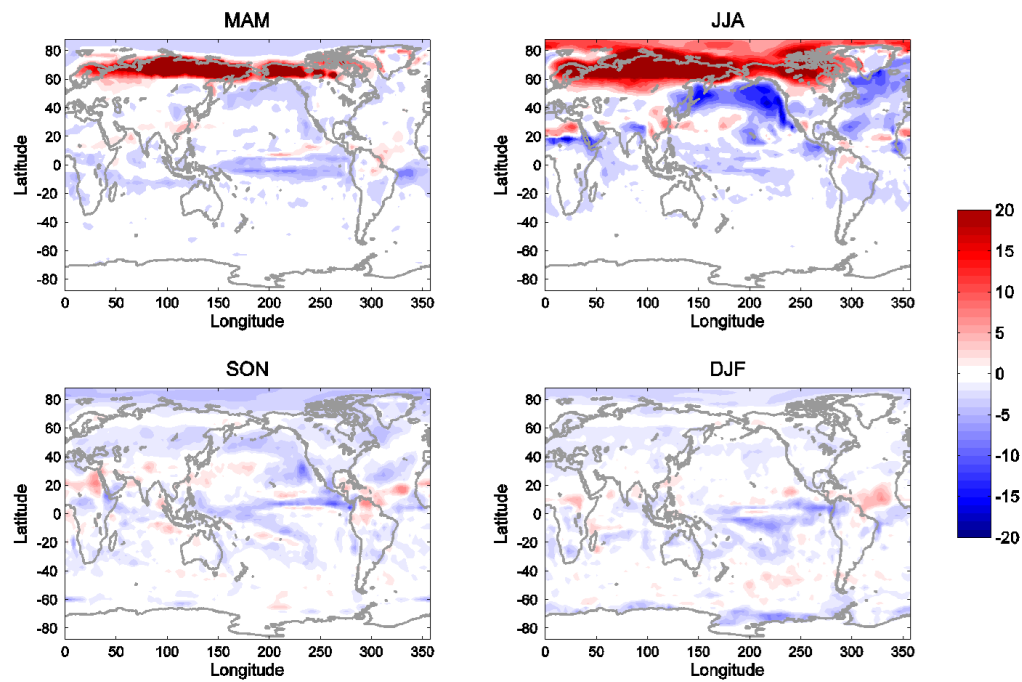


Figure 18 Seasonal map of top-of- atmospheric energy budget (TOT NET in W/m^2). Red and blue corresponds to warming and cooling the atmosphere.

SWCF

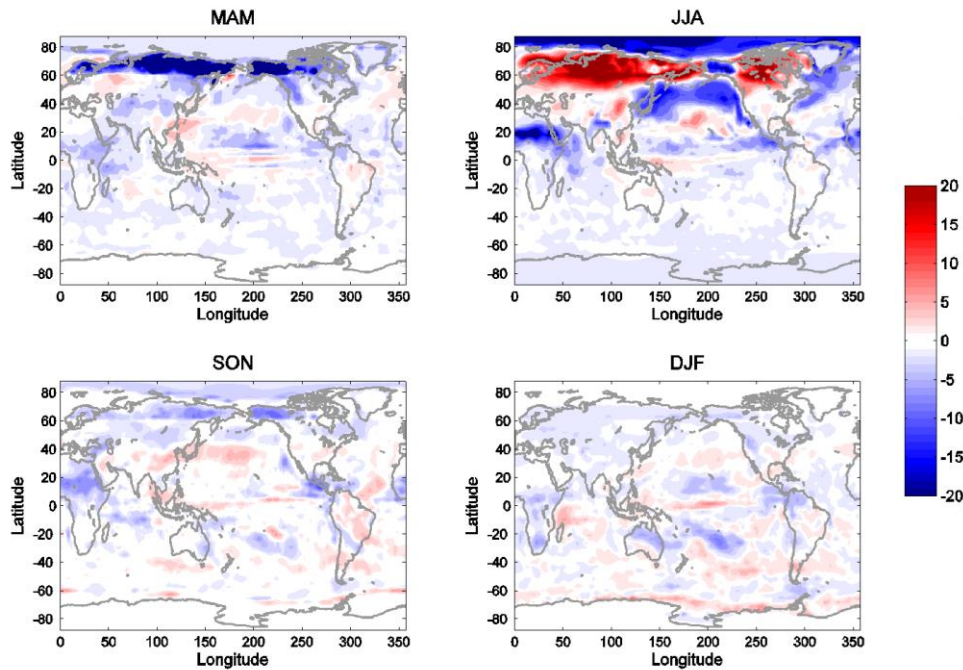


Figure 19 Seasonal maps of short wave cloud forcing (SWCF in W/m^2). Red and blue corresponds to warming and cooling the atmosphere.

SFC NET

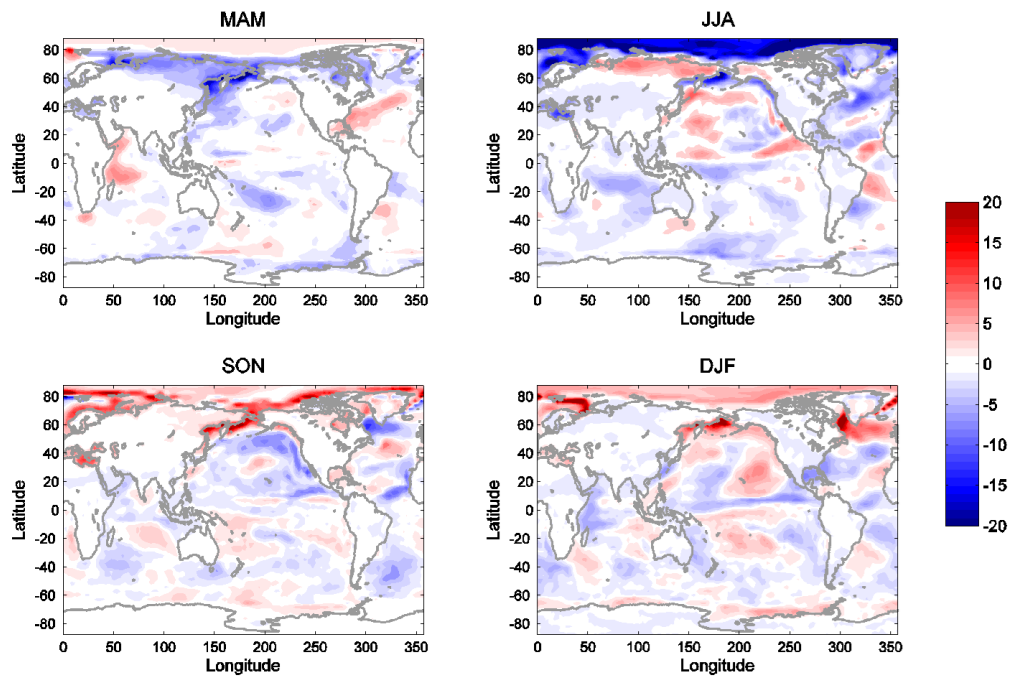


Figure 20 Seasonal map of surface energy budget (SFC NET in W/m^2). Red and blue corresponds to warming and cooling the atmosphere.

TOA SW_{clear}

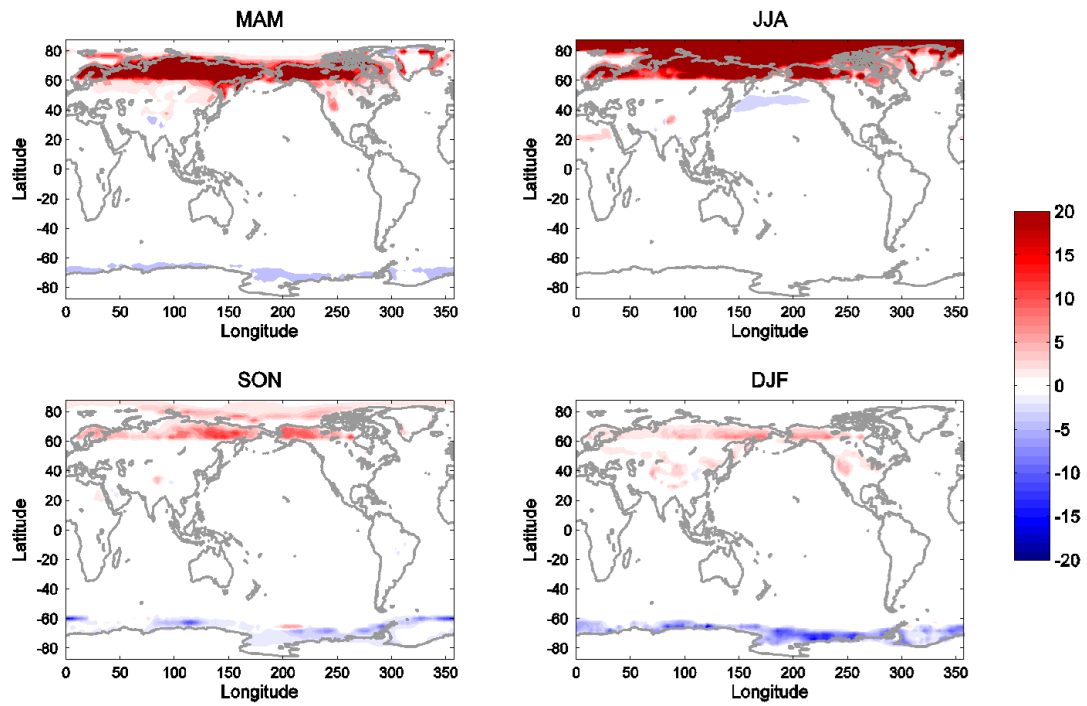


Figure 21 Seasonal map of TOA SW in clear sky (W/m^2). Red and blue corresponds to warming and cooling the atmosphere

Chapter 5. Conclusions

We study the effect of Arctic greening on the seasonality of polar amplification and ITCZ shift using CAM3 coupled to mixed layer ocean and CLM3 with prescribed vegetation type.

In the local effect of Arctic greening, the effect of CO₂ doubling is compared with the effect of Arctic vegetation type change. In particular, shrub and grass poleward of 60°N are changed to boreal forest, which is a potential scenario under double CO₂ suggested by JSJ11. Even though vegetation is changed over small area, its effect on the polar temperature is comparable to CO₂ doubling. In the annual-mean, the lower tropospheric temperature response poleward of 60°N to Arctic vegetation type change is 60% of that to CO₂ doubling. Hence, the Arctic vegetation type change will amplify the regional warming due to CO₂ increase, although, as stated in Section 3, the exact magnitude of the response would be sensitive to the experiment setup. However, the qualitative effect of Arctic greening on the phase shift of peak Arctic warming, which is the focus of our study, would be a robust feature.

Even though vegetation is changed all year long, its ability to reduce surface albedo is maximized in June when the incoming solar radiation reaches maximum over the Arctic. Also, evapotranspiration is enhanced the most in the summer with the highest photosynthesis rate, leading to the largest increase in water vapor and consequently the greenhouse effect. Conversely, from November to January, the solar radiation barely reaches the Arctic, so that vegetation change has little impact on the Arctic temperature. Hence, although vegetation is increased throughout the year, its ability to warm the Arctic is confined to boreal summer because of large seasonality of insolation. Therefore, the peak of Arctic warming that appears in November when doubling of CO₂ is considered in isolation shifts to August when the resulting Arctic vegetation change is additionally taken into account, leading to a weaker seasonality in the Arctic amplification.

In the remote effect of Arctic greening, the heating over the Arctic is balanced by southward cross equatorial atmospheric energy flux. Since in the tropics the energy is transported mostly by the Hadley circulation, which transports moisture by its lower branch, the ITCZ is shifted to the south in the annual mean. However, the seasonality of ITCZ shifts can be different with annual ITCZ shifts.

As Little sunlight reaching the Arctic in SON and DJF, the heating resulting from albedo reduction is smaller a factor of 10, compared with the other seasons. In SON, the cooling from the reduction of SWCF, surface SH, and clear sky upwelling LW in the North Pacific, overcompensates the Arctic heating caused by vegetation change. Hence, Hadley circulation transports energy northward, and the ITCZ is shifted southward in SON.

This study suggests that vegetation change over the Arctic can impact not only on local area but also remote area, and the effect of Arctic greening on the ICTZ shift depends also significant on the seasons due to polar night.

Although there is uncertainty in the potential vegetation change, we expect details of vegetation will only affect the magnitude of the response while holding the qualitative results the same. The present study emphasizes the importance of improving vegetation parameterizations to raise precision of climate change projections.

References

1. Bintanja, R., & Van der Linden, E. C. (2013). The changing seasonal climate in the Arctic. *Scientific reports*, 3, doi:10.1038/srep01556.
2. Broccoli, A., K. Dahl, & R. Stouffer, 2006: Response of the ITCZ to Northern Hemisphere cooling. *Geophysical Research Letters*, 33 (1), L01 702, doi:DOI10.1029/2005GL024546.
3. Bunn, A. G., & S. J. Goetz (2006). Trends in Satellite-Observed Circumpolar Photosynthetic Activity from 1982 to 2003: The Influence of Seasonality, Cover Type, and Vegetation Density. *Earth Interactions*, 10(1).
4. Chapin, F., M. Sturm, M. Serreze, J. McFadden, J. Key, A. Lloyd, A. McGuire, T. Rupp, A. Lynch, & J. Schimel (2005). Role of land-surface changes in Arctic summer warming. *Science*, 310(5748), 657-660.
5. Chen, H., Zhou, T., Neale, R. B., Wu, X., & Zhang, G. J. (2010). Performance of the new NCAR CAM3. 5 in East Asian summer monsoon simulations: Sensitivity to modifications of the convection scheme. *Journal of Climate*, 23(13), 3657-3675.
6. Collier, J. C., & Zhang, G. J. (2007). Effects of increased horizontal resolution on simulation of the North American monsoon in the NCAR CAM3: an evaluation based on surface, satellite, and reanalysis data. *Journal of climate*, 20(9), 1843-1861.
7. Collins, W. D., P. J. Rasch, B. A. Boville, J. J. Hack, J. R. McCaa, D. L. Williamson, J. T. Kiehl, B. Briegleb (2004), Description of the NCAR community atmosphere model (CAM 3.0), Tech. Rep. NCAR TN-464+STR, National Center for Atmospheric Research, Boulder, Colorado.
8. Collins, W. D., Rasch, P. J., Boville, B. A., Hack, J. J., McCaa, J. R., Williamson, D. L., ... & Zhang, M. (2006). The formulation and atmospheric simulation of the Community Atmosphere Model version 3 (CAM3). *Journal of Climate*, 19(11), 2144-2161.
9. Francis, J. A., & Vavrus, S. J. (2012). Evidence linking Arctic amplification to extreme weather in mid-latitudes. *Geophysical Research Letters*, 39(6).

10. Gent, P. R., Yeager, S. G., Neale, R. B., Levis, S., & Bailey, D. A. (2010). Improvements in a half degree atmosphere/land version of the CCSM. *Climate Dynamics*, 34(6), 819-833.
11. Hwang, Y. T., & Frierson, D. M. (2013). Link between the double-Intertropical Convergence Zone problem and cloud biases over the Southern Ocean. *Proceedings of the National Academy of Sciences*, 110(13), 4935-4940.
12. Hurrell, J. W., Hack, J. J., Phillips, A. S., Caron, J., & Yin, J. (2006). The dynamical simulation of the Community Atmosphere Model version 3 (CAM3). *Journal of climate*, 19(11), 2162-2183.
13. Intergovernmental Panel on Climate Change (2007). Climate Change 2007: The Physical Science Basis. Contribution of Working Group I to the Fourth Assessment Report of the Intergovernmental Panel on Climate Change, edited by S. Solomon et al., Cambridge Univ. Press, Cambridge, U. K.2244.x.
14. Jeong, S.-J., C.-H. Ho, T.-W. Park, J. Kim, & S. Levis (2011). Impact of vegetation feedback on the temperature and its diurnal range over the Northern Hemisphere during summer in a 2× CO₂ climate. *Climate dynamics*, 37(3-4), 821-833, doi:10.1029/2007GL031447.
15. Jeong, S.-J., C.-H. Ho, H.-J. Gim, & M. E. Brown (2011). Phenology shifts at start vs. end of growing season in temperate vegetation over the Northern Hemisphere for the period 1982–2008. *Global Change Biology*, 17(7), 2385–2399, doi:10.1111/j.1365-2486.2011.02397.x.
16. Kang, S. M., Held, I. M., Frierson, D. M., & Zhao, M. (2008). The response of the ITCZ to extratropical thermal forcing: Idealized slab-ocean experiments with a GCM. *Journal of Climate*, 21(14), 3521–3532.
17. Kang, S. M., Frierson, D. M., & Held, I. M. (2009). The tropical response to extratropical thermal forcing in an idealized GCM: The importance of radiative feedbacks and convective parameterization. *Journal of the Atmospheric Sciences*, 66(9), 2812-2827.
18. Levis, S., G. Bonan, M. Vertenstein, & K. Oleson (2004). The Community Land Model's dynamic global vegetation model (CLM-DGVM): Technical description and user's guide, NCAR Tech. Note TN-459+ IA, 50.

19. Loranty, M. M., Goetz, S. J., & Beck, P. S. (2011). Tundra vegetation effects on pan-Arctic albedo. *Environmental Research Letters*, 6(2), 024014.
20. Liu, X., Penner, J. E., Ghan, S. J., & Wang, M. (2007). Inclusion of ice microphysics in the NCAR Community Atmospheric Model version 3 (CAM3). *Journal of Climate*, 20(18), 4526-4547.
21. Lu, P., & J. P. McCreary, 1995: Influence of the ITCZ on the flow of thermocline water from the subtropical to the equatorial Pacific Ocean. *Journal of Physical Oceanography*, 25, 3076–3088.
22. Manabe, S., & R. J. Stouffer (1980). Sensitivity of a global climate model to an increase of CO₂ concentration in the atmosphere. *Journal of Geophysical Research*, 85, 5529–5554.
23. Notaro, M., Vavrus, S., & Liu, Z. (2007). Global vegetation and climate change due to future increases in CO₂ as projected by a fully coupled model with dynamic vegetation. *Journal of Climate*, 20(1), 70-90, doi:10.1175/JCLI3989.1.
24. Oleson, K. W., et al. (2004), Technical description of the Community Land Model (CLM), Tech. Rep. NCAR TN-461+STR, National Center for Atmospheric Research, Boulder, Colorado.
25. Pearson, R. G., Phillips, S. J., Loranty, M. M., Beck, P. S., Damoulas, T., Knight, S. J., & Goetz, S. J. (2013). Shifts in Arctic vegetation and associated feedbacks under climate change. *Nature Climate Change*, 3, 673–677.
26. Pithan, F., & Mauritsen, T. (2014). Arctic amplification dominated by temperature feedbacks in contemporary climate models. *Nature Geoscience*, 7, 181-184, doi:10.1038/ngeo2027.
27. Potter, C., Li, S., & Crabtree, R. (2013). Changes in Alaskan tundra ecosystems estimated from MODIS greenness trends, 2000 to 2010. *Journal of Geophysics & Remote Sensing*, 2, 1-7.
28. Screen, J. A., & Simmonds, I. (2010). The central role of diminishing sea ice in recent Arctic temperature amplification. *Nature*, 464(7293), 1334-1337, doi:10.1038/nature09051.
29. Seo, J., Kang, S. M., & Frierson, D. M. (2014). Sensitivity of intertropical convergence zone movement to the latitudinal position of thermal forcing. *Journal of Climate*, 27(8), 3035-3042.

30. Serreze, M. C., & R. G. Barry (2011). Processes and impacts of Arctic amplification: A research synthesis. *Global and Planetary Change*, 77(1–2), 85–96, doi:10.1016/j.gloplacha.2011.03.004.
31. Sturm, M., C. Racine, & K. Tape (2001). Increasing shrub abundance in the Arctic. *Nature*, 411, 546–547.
32. Swann, A. L., I. Y. Fung, S. Levis, G. B. Bonan, & S. C. Doney (2010). Changes in Arctic vegetation amplify high-latitude warming through the greenhouse effect. *Proceedings of the National Academy of Sciences*, 107(4), 1295–1300.
33. Swann, A. L., I. Y. Fung, & J. C. Chiang (2012). Mid-latitude afforestation shifts general circulation and tropical precipitation. *Proceedings of the National Academy of Sciences*, 109(3), 712–716.
34. Swann, A. L., I. Y. Fung, Y. Liu, & J. C. Chiang (2014). Remote vegetation feedbacks and the mid-Holocene Green Sahara. *Journal of Climate*, doi:10.1175/JCLI-D-13-00690.1.
35. Tape, K., M. Sturm, & C. Racine (2006). The evidence for shrub expansion in northern Alaska and the Pan-Arctic. *Global Change Biology*, 12(4), 686–702.
36. Winton, M. (2006). Amplified Arctic climate change: What does surface albedo feedback have to do with it? *Geophysical Research Letters*, 33(3), L03701, doi:10.1029/2005GL025244.
37. Xu, L., Myneni, R. B., Chapin Iii, F. S., Callaghan, T. V., Pinzon, J. E., Tucker, C. J., ... & Stroeve, J. C. (2013). Temperature and vegetation seasonality diminishment over northern lands. *Nature Climate Change*, 3, 581–586.
38. Zhang, G. J., & Song, X. (2009). Interaction of deep and shallow convection is key to Madden Julian Oscillation simulation. *Geophysical Research Letters*, 36(9).